processes

MDPI

Article

Theoretical Simulation of the Resistivity and Fractured–Cavernous Structures of Carbonate Reservoirs

Zhaohui Zhang [1,2,3,*], Chuqiao Gao [4], Yongde Gao [5], Chunzhen Niu [1] and Shenglun Ma [1]

1 School of Geology and Mining Engineering, Xinjiang University, Urumqi 830046, China; ncz0323@126.com (C.N.); mashenglun010@163.com (S.M.)
2 Key Laboratory of Petroleum Resources Research, Lanzhou 730020, China
3 Northwest Institute of Eco-Environment and Resources, Chinese Academy of Sciences, Lanzhou 730020, China
4 College of Geophysics and Petroleum Resources, Yangtze University, Wuhan 430100, China; gaocq@vip.163.com
5 Zhanjiang Branch, CNOOC Limited, Zhanjiang 524057, China; gyongde2008@163.com
* Correspondence: zhangzhaohui@xju.edu.cn

Abstract: Recently, theoretical modeling based on rock physics has emerged as a pivotal approach to studying the resistivity of complex fractured–cavernous microstructures. In this work, to study the effects of fractured–cavernous structures on carbonate reservoir resistivity, electrical conductivity models were developed based on the effective medium theory and Ohm's Law, and theoretical simulations were performed to examine how the porosity and resistivity of the rock matrix, the formation water resistivity, and the parameters of the fractured–cavernous microstructure affect the resistivity of rocks saturated with petroleum or water. Furthermore, the modeling results revealed the specific relationships between these factors in petroleum-saturated and water-saturated rocks. For vuggy reservoirs, a significant negative correlation between throat diameter and resistivity was revealed when variations in the rock matrix and formation water resistivity were negligible. Furthermore, the pore shape—especially the extension of pores in the direction of the current—severely reduced the resistivity of petroleum-saturated rocks. For fractured reservoirs, the porosity and resistivity of the rock matrix were the primary factors affecting resistivity, with the fracture inclination angle and width also exhibiting pronounced effects on the resistivity of water-saturated rocks. The rock cementation exponent was much smaller when the matrix pores were interconnected through fractures than when they were interconnected through throats. The findings reveal that the effects of the structural parameters of fractured–cavernous carbonate reservoirs on reservoir resistivity differ between petroleum-saturated and water-saturated rocks. The conventional Archie's equation is insufficient for evaluating fluid saturation in carbonate reservoirs. A saturation evaluation model with a variable rock cementation exponent tailored to the specific reservoir type should thus be developed.

Keywords: carbonate reservoirs; geologic model; theoretical simulation; resistivity

check for updates

Citation: Zhang, Z.; Gao, C.; Gao, Y.; Niu, C.; Ma, S. Theoretical Simulation of the Resistivity and Fractured–Cavernous Structures of Carbonate Reservoirs. *Processes* **2024**, *12*, 43. https://doi.org/10.3390/pr12010043

Academic Editors: Junjian Zhang, Zhenzhi Wang and Carlos Sierra Fernández

Received: 28 November 2023
Revised: 19 December 2023
Accepted: 21 December 2023
Published: 23 December 2023

1. Introduction

Approximately 60% of global oil and gas reserves were developed in carbonate reservoirs, and many of the world's high-yielding oil and gas reservoirs are associated with carbonate rocks [1–6]. In China, carbonate reservoirs predominantly occur in the Cambrian and Ordovician formations of the Tarim Basin; the Sinian, Cambrian, Devonian, Carboniferous, and Triassic periods of the Sichuan Basin; and the Ordovician formation of the Ordos Basin [7]. Carbonate reservoirs possess a variety of pore spaces, which can be classified into four types: porosity, caves, throats, and fractures [8–13]. Depending on the type and combination of these pore spaces, carbonate reservoirs are categorized into vuggy, fractured, fractured–vuggy, and cavern types [12,13]. Due to their intense heterogeneity, carbonate reservoirs exhibit features of secondary porosity, including dissolution-enhanced fractures and vugs, making their microscopic pore structures exceedingly complex [6,14,15]. These complex fractured–cavernous structures in carbonate reservoirs result in inexplicable resistivity response patterns [16–18], such as numerous layers with anomalously high resistivity, dense layers with low resistivity, and water-bearing layers with high resistivity. Hence, examining the effects of these fractured–cavernous structures on the resistivity of geofluid-saturated rocks is important to deepen the understanding of their resistivity response patterns, identify their fluid properties, and evaluate their fluid saturation state during the exploration and development of complex fractured–cavernous carbonate hydrocarbon reservoirs.

Physical experiments and theoretical simulations are two fundamental approaches in rock physics research [11,18–24]. When physical experiments or the observation of certain parameters in specific rock media become challenging, theoretical simulations can offer advantages. Due to the pronounced heterogeneity typically exhibited by carbonate reservoirs, obtaining representative core samples with diverse fracture characteristics (e.g., fracture width, dip angle, wettability, and fluid content) remains challenging under current experimental conditions. Furthermore, it is particularly challenging to control variables such as pore shape, pore size, pore–throat radius ratio, thickness of the fluid film on the particle surface, and fluid-filling status when studying the electrical properties of rocks. Given these constraints, theoretical simulation is indispensable in studying the fractured–cavernous structures of reservoirs. Considering the significant differences in conductivity mechanisms between the pores and fractures of carbonate reservoirs [4,8,15,20,25], in this study, the responses of deep laterolog resistivity under various structural parameters of pores and fractures in the Ordovician carbonate reservoirs of the Yingshan Formation in the Tazhong area of the Tarim Basin were theoretically simulated. This yielded significant insights into the effects of fractured–cavernous structures on rock resistivity.

For vuggy porosity, numerous conductivity models have been proposed, including the dual-porosity model based on a mechanism of series and parallel conduction [26–38], the tri-porosity model [29,30], and the fractal model [31,32]. A porosity model based on the effective medium theory has also been developed [33]. The dual-porosity and tri-porosity models offer innovative approaches to interpreting resistivity well logging data. However, it remains challenging to determine parameters for the effective medium theory-based conductivity model, limiting its practical applications. To enhance numerical simulations of the conductivity of carbonate reservoirs, a variety of pore structure models based on real-world structures have been proposed, including the capillary bundle model [34,35], the tortuosity model [36,37], the pore network model [38,39], and the percolation network model [40]. Based on the analysis of these conductivity and physical models, this study introduces a simplified physical model by employing the effective medium theory [41,42] and the pore network model [21,28,38,43] to simulate the effects of pore and throat sizes, shapes, porosities, and water film thickness on the resistivity of rocks saturated with two-phase fluids.

Previous research on the electrical properties of fractured reservoir rocks primarily focuses on numerical simulations of dual laterolog responses [4,24,44,45]. The physical models under consideration include those for singular fractures at 0° and 90° [46,47] and those for fractures with arbitrary orientations [44,48–51]. These studies underscore the effects of base rock resistivity, fracture inclination angle, and fracture width on dual laterolog resistivity. However, they often overlook factors such as fluid properties, rock cementation, and wettability and fail to consider the relationships between fracture orientation, tool detection depth, and borehole radius. Building on these prior studies, new physical fracture models for three geometric relationships were established to theoretically simulate deep laterolog resistivity under various stratigraphic conditions, providing support for the evaluation of fractured reservoirs.

2. Conductivity Models of Carbonate Reservoirs

2.1. Porous Reservoirs

For the Ordovician carbonate porous reservoirs of the Yingshan Formation in the Tazhong area of the Tarim Basin, dissolution pores are the main pore spaces [30,52–54], followed by intra-granular pores, inter-granular pores, inter-crystalline pores, and a few micropores. In these reservoirs, fractures are not well developed; thus, throats serve as the primary seepage channels for geofluids, and they also act as electrically conductive paths. Considering the conductive characteristics of these pores and structures, previous models [21,43] were improved, and a new conductivity model was established in this study. The proposed model is composed of three modules: a model describing the micropore structure of rocks, a model describing the theoretical resistivity of basic units, and a model describing the effective medium conductivity.

The micropore structure of rocks is composed of two parts: throats and pores. Throats are represented by rotating cylinders in the model, while pores are depicted as rectangular prisms. The model parameters include the throat diameter and length, along with the pore width, height, and length (Figure 1a). A single throat combined with a pore constitutes a basic unit of the pore network. The overall distribution network of pores and throats can be represented by the throat radius distribution function determined by actual capillary pressure data.

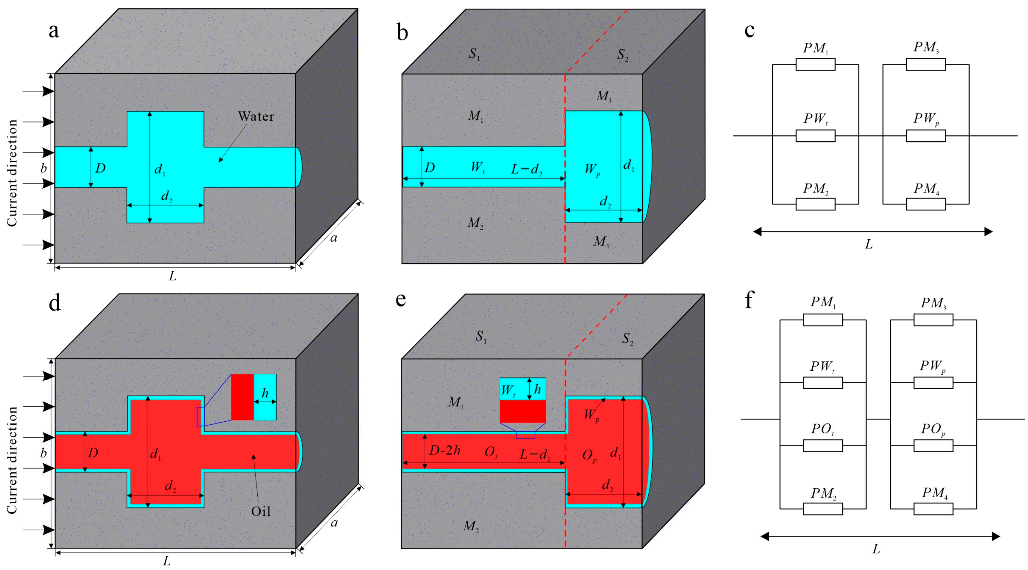

Figure 1. (**a**,**d**) Geologic models of vuggy reservoirs saturated with water (**a**) and oil (**d**). (**b**,**e**) Corresponding conductivity models. (**c**,**f**) The equivalent resistance models of vuggy reservoirs. The model parameters are marked and described as follows: a, b, and L are the width, height, and length of the modeled rock, respectively, in μm; D is the diameter of the throat, in μm; d_1 is the width and height of the pore (perpendicular to the direction of the current), in μm; d_2 is the length of the pore (along the direction of the current), in μm; and h is the water film thickness, in μm. The symbols are described as follows: W_t is the throat water; W_p is the pore water; O_t is the throat oil; O_p is the pore oil; M_1 is the rock matrix block 1 located in the upper part of the throat; M_2 is the rock matrix block 2 located in the lower part of the throat; M_3 is the rock matrix block 3 located in the upper part of the pore; M_4 is the rock matrix block 4 located in the lower part of the pore; S_1 is the throat and surrounding rock matrix module; S_2 is the pore and surrounding rock matrix module; PM_1, PM_2, PM_3, and PM_4 are the equivalent resistance of rock matrix blocks 1, 2, 3, and 4, respectively; PW_t, and PO_t are the equivalent resistance of throat water and oil, respectively; and PW_p and PO_p are the equivalent resistance of pore water and oil, respectively.

The resistivity of the basic units in the pore network model is defined by Ohm's Law. The model posits that the matrix is in parallel electrical connection with the pores and throats, while the pores and throats aligned in the direction of the current are electrically connected in series. When the medium contains two fluid phases (oil and water), the conduction pathway in hydrophilic rocks is thought to be the water films on the inner-wall surfaces of the pores and throats, and the thickness of the water film serves as a model parameter. To simulate the displacement of the wetting phase (formation water) by the non-wetting phase (oil) in hydrophilic rocks, we assume that the displacement process is controlled by capillary pressure, the non-wetting phase first enters the pores with relatively large radii, and a water film always exists on the surface of the rock matrix. According to the effective medium theory [41,55], rocks saturated with two-phase fluids can be considered effective media. The conductivity of the basic units in the effective medium network can represent the conductivity of the entire network.

Mathematical models were developed for two scenarios of pore fluids, as elaborated below.

(1) Rock pores and throats are saturated with water.

Assuming that the rock pores and throats are saturated with water, the geological model depicted in Figure 1a was transformed into a conductivity model (Figure 1b) based on the effective medium theory and Ohm's Law. In the direction of the current, the rock resistance in this model is the series resistance of modules S_1 and S_2. The resistance of module S_1 is the parallel resistance of matrix block M_1, throat water W_t, and matrix block M_2. The series and parallel circuits are according to Kirchhoff's laws. Similarly, the resistance of module S_2 is the parallel resistance of block matrix M_3, pore water W_p, and matrix block M_4. The equivalent resistance model is shown in Figure 1c. The rock resistance in this model is derived based on Ohm's Law:

$$P = \frac{L - d_2}{\frac{\pi\left(\frac{D}{2}\right)^2}{R_w} + \frac{ab - \pi\left(\frac{D}{2}\right)^2}{R_s}} + \frac{d_2}{\frac{{d_1}^2}{R_w} + \frac{ab - {d_1}^2}{R_s}}, \quad (1)$$

where P is the rock resistance, in Ω; R_w and R_s are the resistivities of formation water and the rock matrix, respectively, in Ω.m; a, b, and L are the width, height, and length of the modeled rock, respectively, in µm; D is the diameter of the throat, in µm; d_1 is the width and height of the pore (perpendicular to the direction of the current), in µm; and d_2 is the length of the pore (along the direction of the current), in µm.

According to the law of resistance, the total rock resistance can be calculated as follows:

$$P = \frac{R_t L}{ab}, \quad (2)$$

where R_t is the resistivity of the modeled rock, in Ω.m.

Substituting Equation (2) into Equation (1) yields an equation for the resistivity of the modeled rock:

$$R_t = \frac{\frac{ab}{L}(L - d_2)}{\frac{\pi\left(\frac{D}{2}\right)^2}{R_w} + \frac{ab - \pi\left(\frac{D}{2}\right)^2}{R_s}} + \frac{\frac{ab}{L} d_2}{\frac{{d_1}^2}{R_w} + \frac{ab - {d_1}^2}{R_s}}. \quad (3)$$

(2) Rock pores and throats are saturated with crude oil.

Assuming a hydrophilic rock, after the oil phase displaces the water phase, water films of uniform thickness exist on the inner-wall surfaces of the pores and throats (Figure 1d). These films serve as the primary conduction pathways, even though the pores and throats are saturated with oil. The conductivity model is presented in Figure 1e. In the direction of the current, the rock resistance in this model is the series resistance of modules S_1 and S_2. The resistance of module S_1 is the parallel resistance of matrix block M_1, the throat water film W_t, the throat oil O_t, and matrix block M_2. The resistance of module S_2 is similar to that of module S_1. The series and parallel circuits are according to Kirchhoff's laws. The equivalent resistance model is shown in Figure 1f. Based on Ohm's Law, the mathematical equation for the resistivity of the rock in this model is derived as follows:

$$R_t = \frac{\frac{ab}{L}(L-d_2)}{\frac{\pi\left(\frac{D}{2}\right)^2-\pi\left(\frac{D}{2}-h\right)^2}{R_w}+\frac{\pi\left(\frac{D}{2}-h\right)^2}{R_0}+\frac{ab-\pi\left(\frac{D}{2}\right)^2}{R_s}}+\frac{\frac{ab}{L}d_2}{\frac{{d_1}^2-(d_1-2h)^2}{R_w}+\frac{\left(d^1-2h\right)^2}{R_0}+\frac{ab-{d_1}^2}{R_s}}, \tag{4}$$

where R_o is the crude oil resistivity, in Ω.m, and h is the thickness of the water film, in μm. The value of R_o is generally in the range of 10^9–10^{16} Ω.m, much larger than the resistivities of the formation water and rock matrix; thus, R_o can be regarded as infinite. Accordingly, Equation (4) can be simplified as:

$$R_t = \frac{\frac{ab}{L}(L-d_2)}{\frac{\pi\left(\frac{D}{2}\right)^2-\pi\left(\frac{D}{2}-h\right)^2}{R_w}+\frac{ab-\pi\left(\frac{D}{2}\right)^2}{R_s}}+\frac{\frac{ab}{L}d_2}{\frac{{d_1}^2-(d_1-2h)^2}{R_w}+\frac{ab-{d_1}^2}{R_s}}. \tag{5}$$

2.2. Fractured Reservoirs

Building upon previous models of singular inclined fractures and inclined slab-like fractures [16,17], we developed three types of fractured formation models according to the geometric relationship between the fracture orientation, borehole radius, and detection depth of the deep lateral resistivity log of the dual laterolog tool: (i) The intersection of the fracture plane with the bottom plane of the electrode column is outside the radial detection depth of the electrode (Figure 2a). The angle between the fracture plane and the bottom plane of the electrode column is the fracture inclination angle θ, in degrees; the vertical distance between the two walls of the fracture represents the fracture width w, in μm; the borehole radius is denoted as r, in m; the radial detection depth of the deep laterolog is r_1, in m; and the height of the cylindrical main current of the deep laterolog is H, in m, which is typically 0.74 m. In all models, the effective conductive medium is analogous to that of a vuggy reservoir. (ii) The intersection is between the borehole radius and the radial detection depth (Figure 2b); and (iii) the intersection is within the borehole radius (Figure 2c). Despite the different geometric relationships described above, these models have the following features in common: First, the tool is centered and aligned with the borehole axis, and there is no drilling mud within the borehole; the borehole is externally surrounded by a uniform, infinitely thick formation (rock matrix). Second, the fracture divides the formation into upper and lower sections and intersects with the borehole. Even when the fracture is fully filled with oil, a water film with thickness h (in μm) remains on the surface of the fracture wall (Figure 2d–f).

(1) When the fracture is saturated with water, the total rock resistance within the detection depth of the electrode is the parallel resistance of the upper matrix block M_u, fracture, and lower matrix block M_l (Figure 2a–c). Theoretical models were developed considering the following three geometric relationships:

   (i) The intersection of the fracture plane with the bottom plane of the electrode column is outside the radial detection depth of the electrode (Figure 2a). In this scenario, the rock resistance expression is given based on Ohm's Law:

$$P = \frac{\ln r_1 - \ln r_2}{\frac{2\pi\omega\cos\theta}{R_w}+\frac{2\pi(H-\omega\cos\theta)}{R_s}}. \tag{6}$$

   Furthermore, the rock resistance can be obtained as follows:

$$P = \frac{R_t(\ln r_1 - \ln r_2)}{2\pi H}. \tag{7}$$

Substituting Equation (6) into Equation (7) gives the following expression for rock resistivity:

$$R_t = \frac{2\pi H}{\frac{2\pi\omega\cos\theta}{R_w} + \frac{2\pi(H-\omega\cos\theta)}{R_s}}. \tag{8}$$

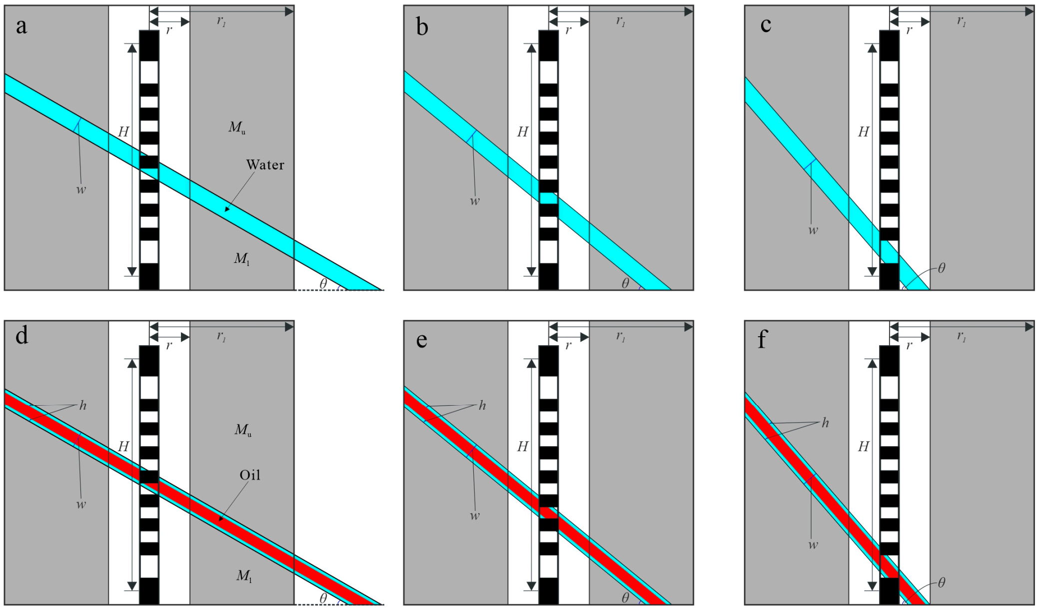

Figure 2. (**a**–**c**) Geologic model of fractured reservoirs saturated with water, where the intersection of the fracture plane with the bottom plane of the electrode column is outside (**a**), between (**b**), and within (**c**) the radial detection depth of the electrode. (**d**–**f**) Geologic model of fractured reservoirs saturated with oil with the intersection outside (**d**), between (**e**), and within (**f**) the radial detection depth of the electrode. The model parameters are marked and described as follows: w is the fracture width, in μm; h is the water film thickness, in μm; r, and r_1 are the borehole radius and radial detection depth of the deep laterolog, respectively, in m; θ is the fracture inclination angle, in degrees; and H is the height of the cylindrical main current of the deep laterolog, in m, which is typically 0.74 m.

(ii) The intersection is between the borehole radius and the radial detection depth (Figure 2b). In this scenario, the rock resistance is given by:

$$P = \frac{\ln r_0 - \ln r}{\frac{2\pi\omega\cos\theta}{R_w} + \frac{2\pi(H-\omega\cos\theta)}{R_s}} + \int_{r_0}^{r_1} \frac{dr_x}{\frac{(2\pi-4\beta)r_x\omega\cos\theta}{R_x} + \frac{2\pi rH-(2\pi-4\beta)r_x\omega\cos\theta}{R_x}}. \tag{9}$$

In Equation (9) and subsequent references, r_0 denotes the distance from the bottom center of the electrode column to the intersection line between the fracture surface and the bottom plane of the electrode column, which is calculated as:

$$r_0 = \frac{H}{2\tan\theta}. \tag{10}$$

In Equation (9), β represents the inclination angle of r_0 relative to the fracture within the integration radius r_x, with the following mathematical expression:

$$\beta = \arccos\frac{H}{2r_x\tan\theta}. \tag{11}$$

Substituting Equation (9) into Equation (7), the rock resistivity is obtained as:

$$R_t = \frac{\frac{2\pi H}{\ln r_1 - \ln r}(\ln r_0 - \ln r)}{\frac{2\pi\omega\cos\theta}{R_w} + \frac{2\pi(H-\omega\cos\theta)}{R_s}} + \frac{2\pi H}{\ln r_1 - \ln r}\int_{r_0}^{r_1} \frac{dr_x}{\frac{(2\pi-4\beta)r_x\omega\cos\theta}{R_x} + \frac{2\pi r H-(2\pi-4\beta)r_x\omega\cos\theta}{R_s}}. \tag{12}$$

(iii) The intersection is within the borehole radius (Figure 2c). In this scenario, the rock resistance is:

$$P = \int_{r_0}^{r_1} \frac{dr_x}{\frac{(2\pi-4\beta)r\omega\cos\theta}{R_w} + \frac{2\pi r H-(2\pi-4\beta)r\omega\cos\theta}{R_s}}. \tag{13}$$

Substituting Equation (13) into Equation (7), the rock resistivity is obtained as:

$$R_t = \frac{2\pi H}{\ln r_1 - \ln r}\int_{r}^{r_1} \frac{dr_x}{\frac{(2\pi-4\beta)r_x\omega\cos\theta}{R_w} + \frac{2\pi r H-(2\pi-4\beta)r_x\omega\cos\theta}{R_s}} \tag{14}$$

(2) When the fracture is saturated with oil, the total rock resistance within the detection depth of the electrode is the parallel resistance of the upper matrix block M_u, fracture w, and lower matrix block M_l (Figure 2d–f). Three theoretical models were developed, considering the following three different geometric relationships:

(i) The intersection of the fracture plane with the bottom plane of the electrode column is outside the radial detection depth of the electrode (Figure 2d). In this scenario, the rock resistance is derived based on Ohm's Law:

$$P = \frac{\ln r_1 - \ln r}{\frac{4\pi h\cos\theta}{R_w} + \frac{2\pi(\omega\cos\theta-2h\cos\theta)}{R_0} + \frac{2\pi(H-\omega\cos\theta)}{R_s}}. \tag{15}$$

The rock resistance can be obtained as follows:

$$P = \frac{R_t(\ln r_1 - \ln r)}{2\pi H}. \tag{16}$$

Substituting Equation (15) into Equation (16), the rock resistivity is obtained as:

$$R_t = \frac{2\pi H}{\frac{4\pi h\cos\theta}{R_w} + \frac{2\pi(\omega\cos\theta-2h\cos\theta)}{R_0} + \frac{2\pi(H-\omega\cos\theta)}{R_s}}. \tag{17}$$

Since R_o is much larger than the resistivities of the formation water and rock matrix, it can be considered to be infinite. Thus, Equation (17) can be simplified as:

$$R_t = \frac{2\pi H}{\frac{4\pi h\cos\theta}{R_w} + \frac{2\pi(H-\omega\cos\theta)}{R_s}}. \tag{18}$$

(ii) The intersection is between the borehole radius and the radial detection depth (Figure 2e). In this scenario, the rock resistance is:

$$P = \frac{\ln r_0 - \ln r}{\frac{4\pi h\cos\theta}{R_w} + \frac{2\pi(\omega\cos\theta-2h\cos\theta)}{R_0} + \frac{2\pi(H-\omega\cos\theta)}{R_s}} + \int_{r_0}^{r_1} \frac{dr_x}{\frac{(2\pi-4\beta)r_x 2h\cos\theta}{R_w} + \frac{2\pi r_x H-(2\pi-4\beta)r_x\omega\cos\theta}{R_s} + \frac{(2\pi-4\beta)r_x(\omega\cos\theta-2h\cos\theta)}{R_0}}. \tag{19}$$

Substituting Equation (19) into Equation (16), the rock resistivity is obtained as:

$$R_t = \frac{\frac{2\pi H}{\ln r_1 - \ln r}(\ln r_0 - \ln r)}{\frac{4\pi h\cos\theta)}{R_w} + \frac{2\pi(\omega\cos\theta-2h\cos\theta)}{R_0} + \frac{2\pi(H-\omega\cos\theta)}{R_s}} + \frac{2\pi H}{\ln r_1 - \ln r}\int_{r_0}^{r_1} \frac{dr_x}{\frac{(2\pi-4\beta)r_x 2h\cos\theta}{R_w} + \frac{2\pi r H-(2\pi-4\beta)r_x\omega\cos\theta}{R_s} + \frac{(2\pi-4\beta)r_x(\omega\cos\theta-2h\cos\theta))}{R_0}}. \tag{20}$$

(iii) The intersection is within the borehole radius (Figure 2f). In this scenario, the rock resistance is:

$$P = \int_{r_0}^{r_1} \frac{dr_x}{\frac{(2\pi-4\beta)r_x 2h\cos\theta}{R_w} + \frac{2\pi rH-(2\pi-4\beta)r_x\omega\cos\theta}{R_s} + \frac{(2\pi-4\beta)r_x(\omega\cos\theta-2h\cos\theta)}{R_0}}. \quad (21)$$

Substituting Equation (21) into Equation (16), the rock resistivity is obtained as:

$$R_t = \frac{2\pi H}{\ln r_1 - \ln r}\int_{r}^{r_1} \frac{dr_x}{\frac{(2\pi-4\beta)r_x 2h\cos\theta}{R_w} + \frac{2\pi rH-(2\pi-4\beta)r_x\omega\cos\theta}{R_s} + \frac{(2\pi-4\beta)r_x(\omega\cos\theta-2h\cos\theta)}{R_0}}. \quad (22)$$

2.3. Rock Cementation Exponent

The rock cementation exponent m (which ranges from 1 to 3) is a key parameter in well logging evaluations for determining the fluid saturation in carbonate reservoirs [4,13,15,29,56]. The relationship between m and the structural parameters of fractured–cavernous rocks was explored using the conductivity model and theoretical simulation equations, providing guidance for calculating fluid saturation in rocks with variable m values. We assumed that in a rock fully saturated with water, the pores are interconnected, showing permeabilities through a fracture with width w, and each pore has a length, width, and height of d_2, d_1, and d_1, respectively. The physical model for a unit volume with edge length L is shown in Figure 3.

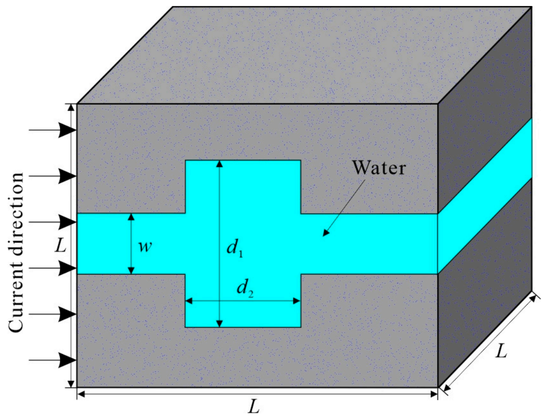

Figure 3. Geologic model of rocks with pores interconnected through fractures. The model parameters are marked and described as follows: L is the width, height, and length of the modeled rock, in μm; w is the fracture width, in μm; d_1 is the width and height of the pore (perpendicular to the direction of the current), in μm; d_2 is the length of the pore (along the direction of the current), in μm.

The volume of porous space in the physical model is:

$$V = {d_1}^2 d_2 + L^2 w - d_1 d_2 w. \quad (23)$$

Assuming that the rock skeleton is not electrically conductive, the rock resistance is:

$$P = R_W\left(\frac{L-d_2}{Lw} + \frac{d_2}{{d_1}^2 + (L-d_1)w}\right). \quad (24)$$

According to the law of resistance, the rock resistivity is:

$$R_t = \frac{PS}{L} = R_W L\left(\frac{L-d_2}{Lw} + \frac{d_2}{{d_1}^2 + (L-d_1)w}\right). \quad (25)$$

The formation factor F is obtained from Archie's equation as follows:

$$F = \frac{R_O}{R_W} = L\left(\frac{L-d_2}{Lw} + \frac{d_2}{{d_1}^2 + (L-d_1)w}\right). \quad (26)$$

The rock porosity in the physical model of Figure 3 is:

$$\varnothing = \frac{V_W}{V} = \frac{{d_1}^2 d_2 + L^2 h_f - d_1 d_2 h_f}{L^3}. \quad (27)$$

Writing Archie's equation as $F = a/\varnothing^m$ and letting the scale factor be a = 1, the rock cementation exponent is obtained as:

$$m = -\frac{\ln\left(\frac{L-d_2}{w} + \frac{d_2}{{d_1}^2+(L-d_1)w}\right)}{\ln\left({d_1}^2 d_2 + h_f - d_1 d_2 w\right)}. \quad (28)$$

When the pores in the rock are interconnected through throats with diameter D, the following equation can be used to calculate the rock cementation exponent m:

$$m = -\frac{\ln\left(\frac{L-d_2}{\pi\left(\frac{D}{2}\right)^2} + \frac{d_2}{{d_1}^2}\right)}{\ln\left({d_1}^2 d_2 + \pi\left(\frac{D}{2}\right)^2 - (1-d_2)\right)} \quad (29)$$

3. Univariate Analysis of the Theoretical Models

The theoretical model expressions reveal that the resistivity of carbonate rocks in vuggy and fractured reservoirs is closely associated with their fractured–cavernous structures. Given the multitude of fractured–cavernous structural parameters, multiple parameters in a single simulation can obscure the distinct effect of each parameter on rock resistivity [4,21,57]. Furthermore, it becomes challenging to identify the primary factor influencing rock resistivity across different reservoir types. Therefore, in the numerical simulations, we began by systematically adjusting a specific parameter and recording the response of resistivity while holding other parameters constant. Subsequently, we generated a cross-plot of the values of the specific parameter versus the corresponding simulated values of rock resistivity, enabling a comprehensive evaluation of the effect of the specific parameter on rock resistivity. This method was applied separately to each fractured–cavernous structural parameter.

3.1. Pore Parameters

Pores and throats are the primary components of the pore system in vuggy reservoirs [11,13,58,59]. When electric currents pass through large pores and small throats, their distribution densities vary, resulting in differential conductivity. In this study, based on the model presented in Figure 1, we used Equations (3) and (5) to simulate the effect of pore and throat structural parameters on the resistivity of rocks saturated with different fluids.

Figure 4a depicts the effect of throat diameter on rock resistivity. The parameters chosen for these models are based on values ranging from 0.002 to 0.01 μm. The parameters were set as follows: pore height d_1 = 0.46 μm; formation water resistivity Rw = 0.02 Ω.m; rock matrix resistivity Rs = 20,000 Ω.m; pore length d_2 = 0.36 μm; and water film thickness h = 0.001 μm. As the throat diameter increased, both the water-saturated and oil-saturated rock resistivity decreased notably. When the throat diameter increased within the range of 0.002–0.004 μm, the resistivity of both water-saturated and oil-saturated rocks declined steeply, and the decrease was more significant in the water-saturated rock resistivity. When D increased in the range of 0.004–0.008 μm, the resistivity continuously decreased, but at a lower rate. When D exceeded 0.008 μm, the decline in resistivity markedly weakened or was not observable at all. The simulation suggests that as the throat diameter increases, the rock resistivity of vuggy reservoirs declines in a triphasic manner: an initial steep decline followed by a steady decline, and finally a marginal decline. This pattern might be associated with the distribution density of the injected current.

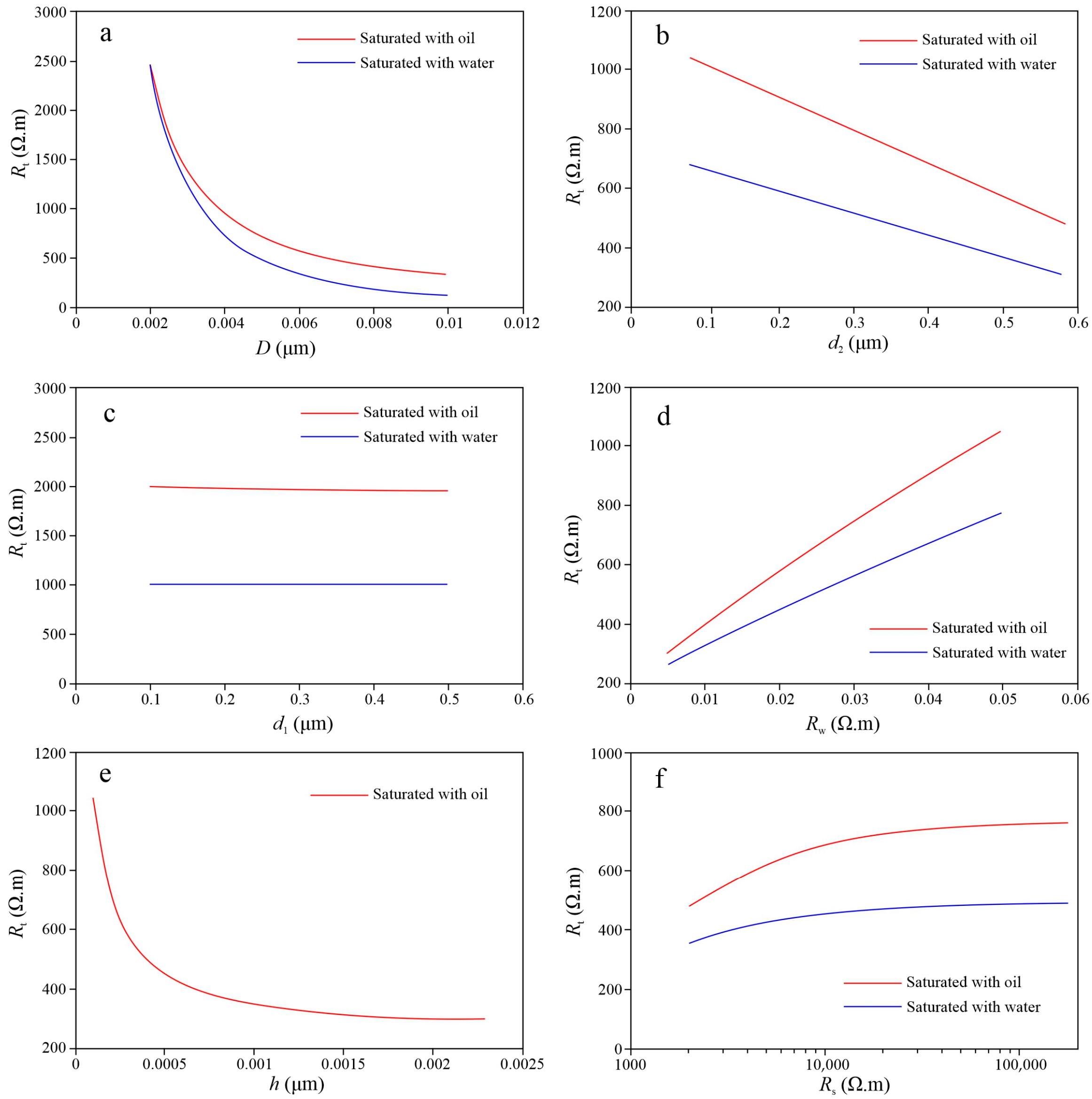

Figure 4. (**a**) Effects of the diameter of the throat, (**b**) the length of the pore (along the direction of the current), (**c**) the width and height of the pore (perpendicular to the direction of the current), (**d**) the resistivity of formation water, (**e**) the water film thickness, and (**f**) the resistivity of rock matrix on the resistivity of vuggy reservoirs.

To investigate the effects of pore size and shape on rock resistivity, the pore dimensions were altered in two directions (along and perpendicular to the direction of the current) to simulate changes in rock resistivity. When the pore length (d_2) was increased in the direction of the current, the simulation results (Figure 4b) indicate a clear linear decrease in resistivity for both water-saturated and oil-saturated rocks. The parameters for this scenario were set as follows: d_1 = 0.46 μm, h = 0.001 μm, D = 0.005 μm, R_w = 0.02 Ω.m, and R_s = 20,000 Ω.m. Notably, the decline in resistivity was more pronounced for oil-saturated rocks, suggesting that changes in pore dimensions have a more significant effect on the resistivity of oil-saturated rocks. Conversely, when the pore width and height (d_1) were increased in the direction perpendicular to the current direction, no significant increase or decrease in resistivity was observed in either the water-saturated or oil-saturated rocks (Figure 4c). For this simulation, the pore length was set to d_2 = 0.36 µm, while the other parameters remained the same as above. The simulation results indicate that only changes in pore dimensions along the direction of the current have a significant effect on reservoir resistivity, which might be associated with the length of the conduction path.

In addition to the sizes and shapes of pores and throats, the formation water resistivity is another factor affecting the resistivity of rocks when their pores and throats are saturated with water or oil (Figure 4d). For this scenario, the parameters were set as follows: d_1 = 0.46 µm, d_2 = 0.36 µm, h = 0.001 µm, D = 0.005 µm, and R_s = 20,000 Ω.m. As the resistivity of the formation water increased, both the water-saturated and oil-saturated rock resistivities displayed notable linear increases. Moreover, the increase in resistivity was more pronounced for rocks with oil-saturated pores and throats, suggesting that the formation water resistivity has a stronger effect on the resistivity of oil-saturated rocks than on that of water-saturated rocks.

The conductivity of a rock with oil-saturated pores and throats depends on the thickness of the water films on the inner walls of the pores and throats. Figure 4e illustrates the effect of water film thickness on the resistivity of oil-saturated rocks. When the water film thickness increased from 0.0001 to 0.0005 µm, the resistivity of oil-saturated rocks decreased sharply. As the water film thickness in the throats further increased to 0.0015 µm, the rock resistivity continued to decline significantly. With further increases in water film thickness, the rock resistivity decreased slightly. Overall, as the water film thickness increased, the resistivity of oil-saturated rocks decreased in a triphasic manner: an initial steep decline followed by a steady decline, and finally a marginal decline. This pattern might be associated with the distribution density of the injected current.

Finally, the effects of rock matrix resistivity on the resistivity of rocks with oil- and water-saturated pores and throats were simulated, as depicted in Figure 4f. The parameters were set as follows: d_1 = 0.46 µm, d_2 = 0.36 µm, h = 0.001 µm, D = 0.005 µm, and R_w = 0.015 Ω.m. The resistivities of both the water-saturated and oil-saturated rocks increased distinctly as the rock matrix resistivity increased, and the effect was more pronounced for oil-saturated rocks. This suggests that rock matrix resistivity has a greater effect on the resistivity of oil-saturated rocks than on that of water-saturated rocks. Moreover, the resistivity response value of reservoir rocks was significantly lower than the resistivity of the rock matrix, indicating the high conductivity of the effective medium in porous systems. These insights suggest that resistivity can indicate not only the degree of pore development but also the characteristics of the contained fluids, in close alignment with Archie's equation [56].

3.2. Fracture Parameters

Fractures serve both as storage spaces for hydrocarbons and as flow pathways [60–63]. Unlike pores and throats, fractures extend considerably in specific directions, are inclined at specific angles, and have well-defined widths [11,15]. Fractures identifiable through core observations and well logging information typically have extension lengths greater than the radial detection depth of the deep laterolog; however, the widths of these fractures are much smaller than the detection depth of the instrument [57]. The fracture surface often intersects at an angle with the current that is injected into the formation by the logging tool, implying that the structural parameters of fractures have significant effects on rock resistivity. We now focus on the prevalent scenario where the fracture surface intersects with the electrode base plane outside of the instrument's detection depth. Based on the models depicted in Figure 2, the resistivities of rocks with water-saturated and oil-saturated fractures were simulated using Equations (8) and (18), respectively.

Figure 5a illustrates the effects of the fracture inclination angle on the resistivities of rocks saturated with water and oil. The parameters were set as follows: w = 40 µm, h = 0.32 µm, R_w = 0.04 Ω.m, and R_s = 2000 Ω.m. As the fracture inclination angle increased, the resistivity of rocks with oil-saturated fractures increased slightly, while the increase in resistivity of rocks with water-saturated fractures was more pronounced. When $\theta < 50°$, the resistivity of rocks with water-saturated fractures gradually increased with increasing fracture inclination angle. However, when $\theta > 50°$, the effect of fracture inclination angle became more significant, and the rock resistivity increased rapidly with increasing inclination angle. Figure 5b shows the effects of fracture width on the resistivity of rocks with water-saturated and oil-saturated fractures for a constant fracture inclination angle. With $\theta = 80°$ and the other parameters remaining unchanged, the resistivity of rocks with oil-saturated fractures remained essentially the same as the fracture width increased, whereas the resistivity of rocks with water-saturated fractures markedly decreased. The simulation results indicate that the fracture inclination angle and fracture width had stronger effects on the resistivity of rocks with water-saturated fractures than on that of rocks containing oil-saturated fractures. This might be related to the distribution of injected current within the effective medium.

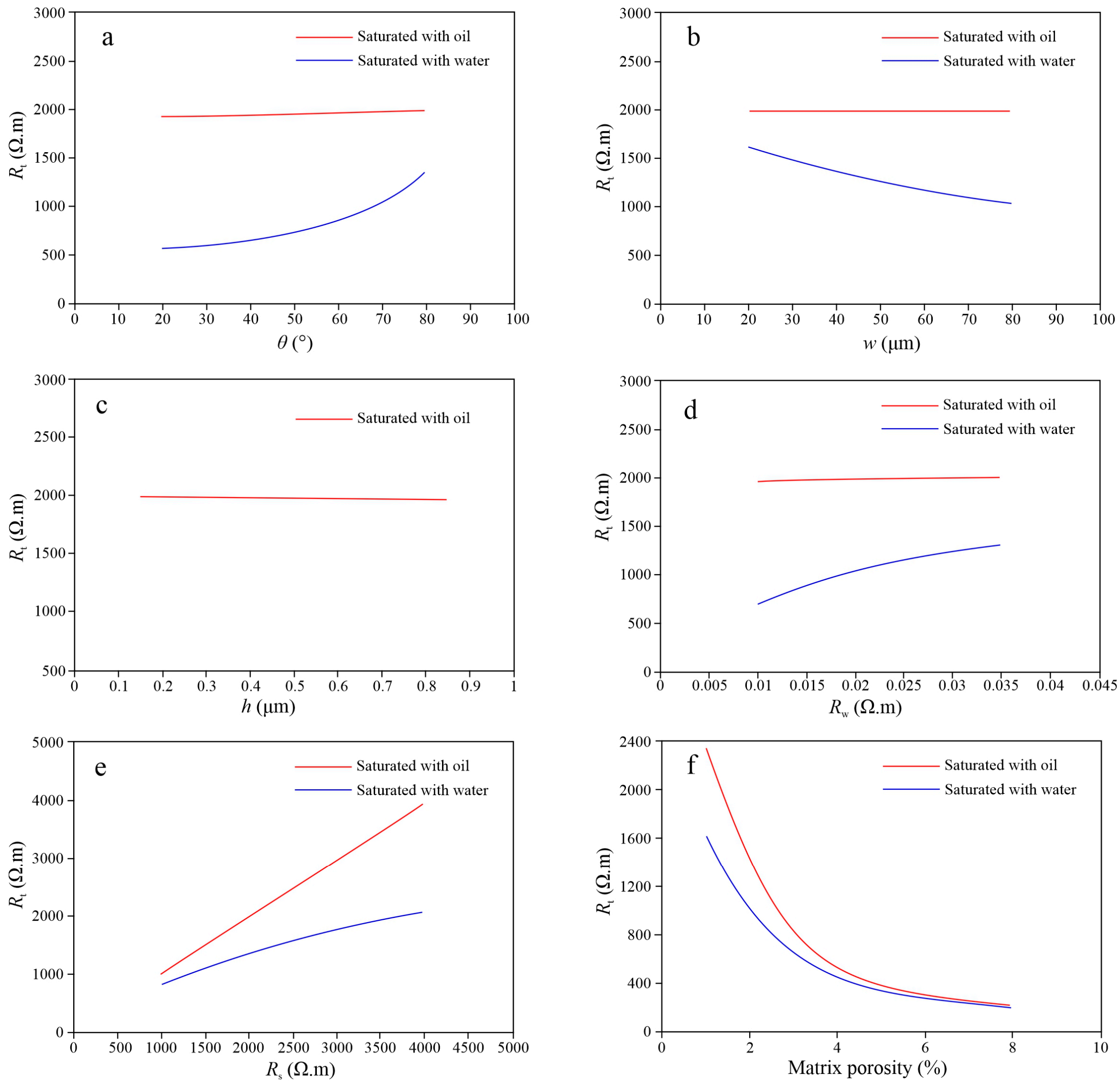

Figure 5. Effects of Fractured–cavernous structural characteristics on the resistivity of fractured reservoirs. (**a**) The fracture inclination angle, (**b**) the fracture width, (**c**) the water film thickness, (**d**) the resistivity of formation water, (**e**) the resistivity of rock matrix, and (**f**) the rock matrix porosity.

For rocks with oil-saturated fractures, in addition to parameters related to fracture development, one must consider whether the presence of water films on the inner walls of the fractures affects resistivity. Figure 5c illustrates the effect of water film thickness on resistivity. When the parameters were set as w = 40 μm, θ = 80°, R_w = 0.04 Ω.m, and R_s = 2000 Ω.m, the resistivity of rocks with oil-saturated fractures decreased slightly as the thickness of the water film increased. Although thin water films possess some conductivity, their limited thickness is insufficient to significantly reduce resistivity.

Figure 5d presents the effect of formation water resistivity on the resistivity of fractured reservoirs. The parameters are set as follows: w = 40 μm, θ = 80°, h = 0.32 μm, and R_s = 2000 Ω.m. As the resistivity of formation water increased, the resistivity of oil-saturated rocks increased slightly, while the increase in resistivity of rocks with water-saturated fractures was more pronounced. When R_w < 0.02 Ω.m, the resistivity of rocks with water-saturated fractures markedly increased with increasing formation water resistivity. However, when R_w > 0.02 Ω.m, the effect of formation water resistivity on the resistivity of rocks with water-saturated fractures became significantly weaker. The simulation results indicate that the effects of formation water resistivity on the resistivity of rocks with water-saturated and oil-saturated fractures are generally minor, especially for rocks with oil-saturated fractures.

In addition to the structural parameters of fractures and the resistivity of formation water, we also conducted theoretical simulations of the effects of rock matrix resistivity on the resistivity of rocks with water-saturated and oil-saturated fractures (Figure 5e). The parameters were set as follows: w = 40 μm, θ = 80°, h = 0.32 μm, and R_w = 0.04 Ω.m. The resistivity of rocks, regardless of whether their fractures were saturated with water or oil, rapidly increased with increasing rock matrix resistivity. This increase was more pronounced for oil-saturated rocks than for water-saturated rocks. However, the rate of change in rock matrix resistivity was essentially the same as that of the resistivity of rocks with oil-saturated fractures. This suggests that fractures have no effect on rock resistivity when they are saturated with oil, which might be related to the distribution of the effective medium.

To comprehensively examine the effects of the rock matrix on the resistivity of fractured reservoirs, the effect of matrix porosity was further simulated. Considering the absence of matrix porosity in the theoretic resistivity model proposed in this study, we first converted the given matrix porosity into R_s using Archie's equation and then substituted it into Equations (1) and (18) to indirectly simulate the effect of matrix porosity on rock resistivity (Figure 5f). In this scenario, the matrix water saturation S_w was 30%, with w = 40 μm, θ = 80°, h = 0.32 μm, and R_w = 0.04 Ω.m. The resistivities of rocks with water-saturated or oil-saturated fractures rapidly decreased as the matrix porosity increased. When the matrix porosity was between 1.5% and 3%, the rock resistivity sharply decreased with increasing matrix porosity. As the matrix porosity increased from 3% to 6%, the reduction in rock resistivity gradually diminished, which is in accordance with previous study results [21,28]. When the matrix porosity exceeded 6%, its effect on rock resistivity became notably weaker. The simulation results indicate that as matrix porosity increases, rock resistivity decreases in a triphasic manner: an initial steep decline followed by a steady decline, and finally a marginal decline. The degree of resistivity reduction was more pronounced for rocks with oil-saturated fractures than those with water-saturated fractures, which might be closely related to the conductive characteristics of the pore system.

4. Discussion

4.1. Changes in Rock Cementation Exponent

Currently, m is mainly determined through experimental measurements [4,11]. However, in the case of complex and highly heterogeneous unconventional reservoirs such as carbonates, volcanic rocks, tight sandstones, and shales, there is an urgent need to establish quantitative relationships between m and the microscopic characteristics [4,35,62,64]. These relationships are essential for obtaining the value of m as it varies with the heterogeneity of the reservoir, thereby enhancing the accuracy of saturation evaluation. In this study, we developed theoretical mathematical models (Equations (28) and (29)) linking the fractured–cavernous structural parameters of carbonate reservoirs to m. The variations in the porosities of porous carbonate reservoirs mainly originate from the large pores, whereas the contributions from micro-fractures and throats are relatively minor. Therefore, within a certain range of rock matrix porosity, both fracture width and throat diameter remain constant, with only the pore size varying. Using the model depicted in Figure 3 and Equation (28) and setting w = 0.003 μm, the changes in m with matrix porosity for the scenario were obtained, where pores are interconnected through fractures (Figure 6a). Using Equation (29) and setting D = 0.03 μm, the changes in m with matrix porosity for the scenario were obtained, where pores are interconnected through throats (Figure 6a). Regardless of whether the pores were interconnected through fractures or throats, m increased with increasing matrix porosity. The rate of increase gradually decreased with matrix porosity, with m tending to stabilize when the matrix porosity exceeded 10%.

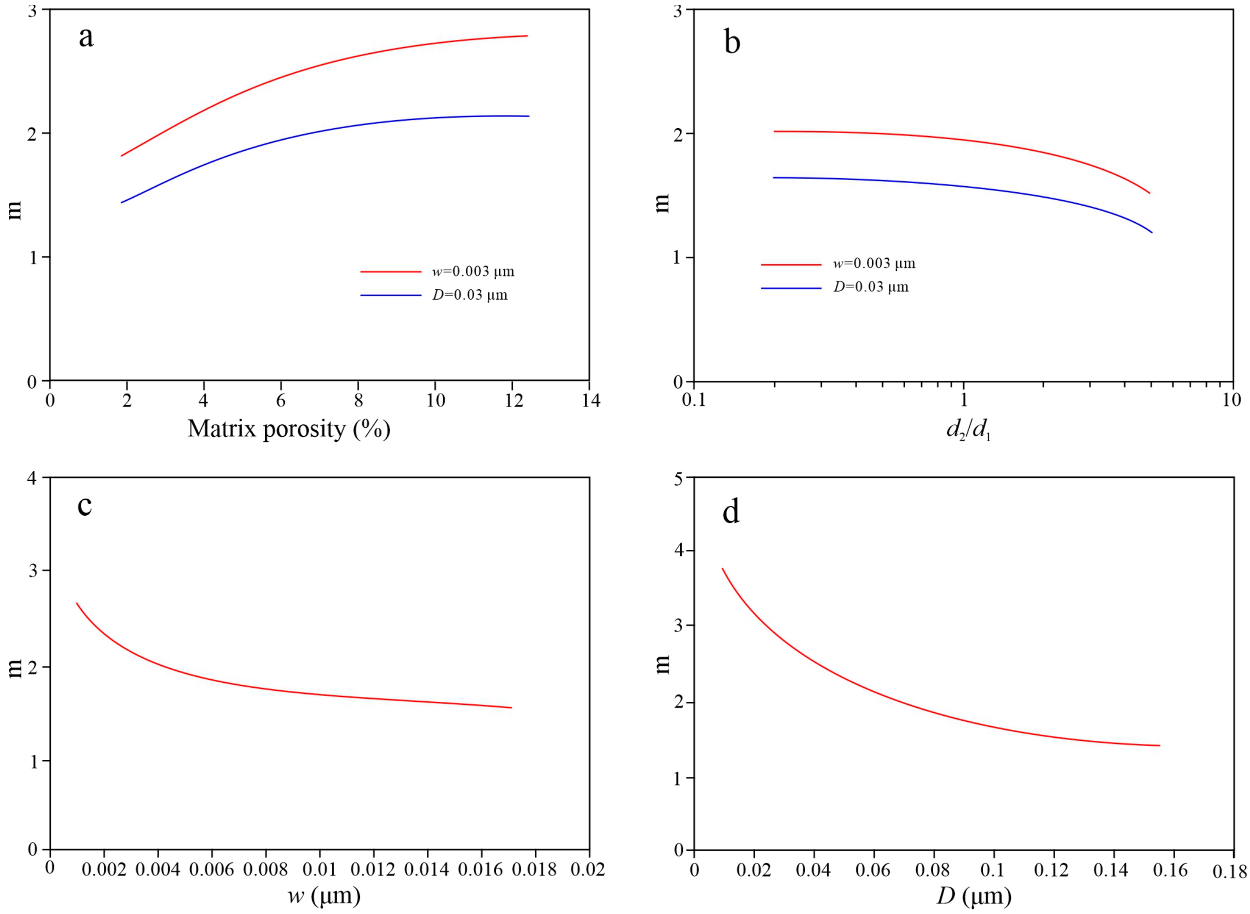

Figure 6. (**a**) Effect of the rock matrix porosity, (**b**) the pore shape, (**c**) the fracture width, and (**d**) the throat diameter on rock cementation exponent m.

The resistivity simulations of porous reservoirs indicate that changing the pore size along and perpendicular to the direction of the electric current results in distinct effects on resistivity (Figure 4b,c). The variation in pore size affects the rock cementation exponent. By keeping the rock porosity constant and varying d_1 and d_2, theoretical simulations were performed to examine the effect of pore shape on m (Figure 6b). The m value gradually decreased as the ratio of d_2 to d_1 increased. When $d_2/d_1 > 1$, the m value decreased rapidly as the ratio increased. Thus, we can infer that m is closely related to the pore shape; for a constant porosity, the larger the value of d_2 in the direction of the current, the smaller the m value.

Keeping the pore size and shape constant, we examined the changes in m with fracture width and throat diameter (Figure 6c,d). As both fracture width and throat diameter increased, the *m* value decreased in a triphasic manner: an initial steep decline followed by a steady decline, and finally a marginal decline. When the rock porosity was held constant and the pores were interconnected through fractures, the value of *m* was small, even though the fracture width was much smaller than the throat diameter. This indicates that in rocks, the capability of fractures to interconnect pores is much greater than that of throats. Hence, when using Archie's equation to calculate the saturation of fractured carbonate reservoirs, the rock cementation exponent *m* should be set slightly lower than the experimentally measured value.

4.2. Effects of Fractured–Cavernous Structural Parameters on Resistivity

Based on the physical models of vuggy and fractured reservoirs along with the principles of resistivity logging methods, the mathematical models of resistivity for different types of reservoirs were established, and univariate simulations were performed (Figures 4 and 5). The results indicate that the effect of each Fractured–cavernous structural parameter on the resistivity varies significantly across different types of reservoirs.

For vuggy reservoirs saturated with either oil or water and with insignificant variations in rock matrix and formation water resistivity (Figure 4), the throat diameter was the primary factor affecting rock resistivity, followed by vug shape (particularly the pore length in the direction of current). Conversely, the pore length perpendicular to the current direction had little effect on resistivity. A comprehensive comparative analysis revealed that the effect of throat diameter on rock resistivity was stronger for water-saturated rocks than for oil-saturated rocks, whereas the other parameters had more pronounced effects on oil-saturated rocks. For the same throat diameter, oil-saturated rocks have more complex conductive pathways than water-saturated rocks, leading to increased variations in rock resistivity. When a vuggy reservoir contains a small number of fractures, the rock resistivity is significantly reduced due to the high conductivity of these fractures, causing the patterns of changes in the resistivity of the vuggy reservoir to be less evident.

Although pore formation is limited in fractured reservoirs, the matrix porosity of the rock remains the primary factor influencing rock resistivity (Figure 5), followed by the matrix resistivity. The inclination angle and width of the fractures had a noticeable effect on rock resistivity when the fractures were saturated with water but virtually no effect when the fractures were saturated with oil. The spatial sizes of the fractures in the reservoirs are much smaller than those of the matrix pores (the former amounting to approximately 1% of the latter); therefore, the spatial sizes of fractures are not sufficient to dictate the overall resistivity of the rock mass.

4.3. Causes of Anomalous Resistivity

In the Tazhong area of the Tarim Basin in western China, the Ordovician carbonate strata consist, from the top to the bottom, of the Sangtamu, Lianglitage, Yijianfang, Yingshan, and Penglaiba Formations. The Yingshan Formation can be divided into the Ying 1, Ying 2, Ying 3, and Ying 4 members from the top to the bottom. The Ying 4 and Ying 3 members are composed of dolomite and grain dolomite. The Ying 2 member is mainly composed of limestone, dolomite, and argillaceous limestone, while the Ying 1 member primarily consists of grainstone and micrite. There are several carbonate reservoirs and caprocks in the Yingshan Formation [65,66].

Figure 7a displays a section of the logging curves of well X of the Ying 2 member in the Tazhong area. This section represents a vuggy reservoir. In the depth range of 4695–4710 m, the computed porosity averaged 2.3%, and the deep laterolog resistivity (RLLD) was 4725 Ω.m, suggesting that this section is an oil-bearing layer. However, production tests for this section had a daily output of 0.23 m^3 of crude oil and 32.88 m^3 of water, classifying it as a typical high-resistivity water-bearing layer—contradictory with respect to the logging interpretation result. The logging curve response characteristics, along with the macro-porosity and saturation parameters, fail to clarify this anomalous phenomenon. To gain insights into this anomaly from the perspective of the microscopic pore structure, we assumed both d_1 and d_2 to be 0.25 μm (i.e., matrix porosity Ø = 0.56%), with R_w = 0.015 Ω.m and R_s = 20,000 Ω.m. Figure 7b illustrates the theoretical simulation of the rock resistivity of the water-bearing layer in relation to the throat diameter. As the throat diameter decreased, the resistivity increased. This may be explained as follows: When the pores are not interconnected, there is no conductive pathway, resulting in a relatively high resistivity that possibly approaches the matrix resistivity of the rock. This suggests that, in such a scenario, the rock resistivity is not influenced by the fluid properties within the pores. As the porosity increased from 1.56% to 3.6% and d_1 and d_2 correspondingly increased from 0.25 to 0.33 μm, the simulated rock resistivity did not decrease significantly (Figure 7b). This further confirms that in the absence of pore connectivity, variations in pore size do not notably influence rock resistivity, and the effect of throat diameter is more pronounced. Formation microresistivity images of this section display numerous small pores, suggesting that the narrowness of the pore throats might be the primary factor contributing to the significantly elevated resistivity of this layer.

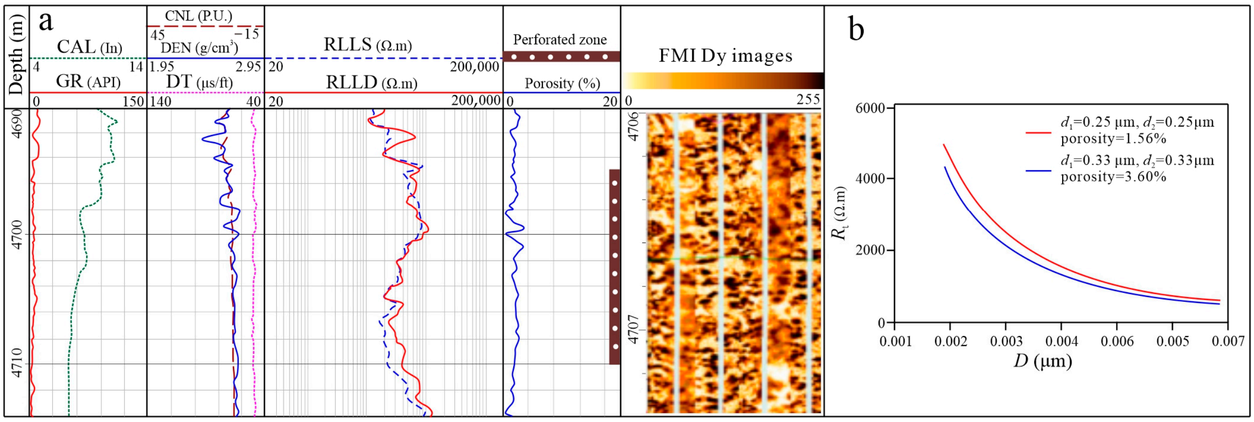

Figure 7. (**a**) Well logging response of a high-resistivity water-bearing layer in well X; and (**b**) the significant effects of throat diameter on the reservoir resistivity.

Figure 8a displays a section of the logging curves of well Y in the Tazhong area of the Tarim Basin, western China. This section represents a fractured reservoir with limited porosity. In the depth range of 5784–5795 m, the computed porosity was less than 2%, and the deep laterolog resistivity (RLLD) was ~200 Ω.m, characterizing it as a typical low-resistivity dense layer. Using the actual parameters of this well and the theoretical Equation (18), we simulated the effect of fracture width on the resistivity of water-saturated rocks (Figure 8b). The simulation parameters were set as follows: θ = 60°, h = 0.32 μm, R_w = 0.04 Ω.m, R_s = 2000 Ω.m, S_w = 50%, and Ø = 1%. The resistivity of dense rocks with small matrix pores decreased significantly as fracture width increased. For carbonate reservoirs with limited porosity, the reservoir resistivity should not differ greatly from the rock matrix resistivity. However, when fractures are formed and saturated with water within the reservoirs, an increase in fracture width would enhance the rock conductivity and thus lead to a substantial reduction in resistivity (Figure 8b); this is a key reason for the low resistivity of dense reservoir rocks. Such characteristics are predominantly found in fractured reservoirs and are relatively less common in vuggy reservoirs and fractured–porous reservoirs.

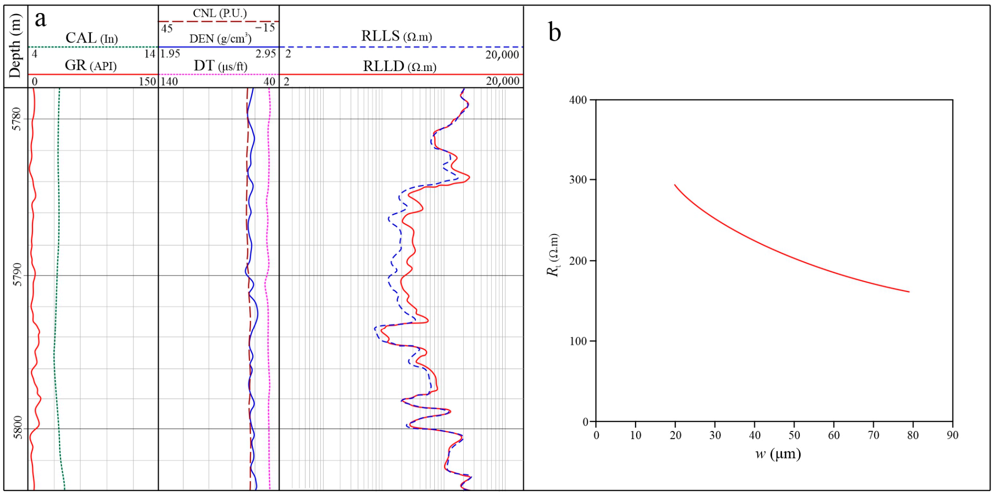

Figure 8. (**a**) Well logging response of a low-resistivity tight layer in well Y; and (**b**) the effects of fracture width on the reservoir resistivity.

4.4. Implications for the Exploration and Development of Oil and Gas in Carbonate Reservoirs

Conductivity is a crucial characteristic of geological formations. Archie's equation intimately connects rock properties, electrical properties, and oil content, making it a fundamental model for calculating formation fluid saturation and a key tool in well logging evaluations. However, the intense heterogeneity of carbonate reservoirs combined with the diverse types of storage spaces they possess result in significant conductivity differences among different pore types. This often leads to anomalies in resistivity curves when interpreting the curves to identify reservoir fluid properties and assess fluid saturation, thereby complicating well logging interpretations. To enhance the accuracy of well logging evaluations, it is imperative to consider the microscopic pore structures based on the type of storage space and harness the strengths of theoretical simulation methods. This approach overcomes the shortcomings of traditional experimental research methods to provide a deeper understanding of how the structural parameters of fractured–cavernous carbonate reservoirs influence resistivity. The results of the theoretical simulations provide a reliable basis for the rational interpretation of anomalous well logging curves and lay a theoretical foundation for calibrating well logging curves against the results of micropore structural analysis of sample sections. Additionally, for corporate technical experts performing well logging and geological evaluations, the findings offer valuable guidance to help facilitate the selection of favorable exploration layers, optimize perforation zones, and modify extraction strategies to ensure the profitability of oil field operations. Finally, the results serve as a useful reference for interpreting resistivity in dense sandstone and shale reservoirs.

Numerous exploration practices reveal that the complexity of the geological conditions in terms of changes in temperature, pressure, mineral composition, and content is closely associated with the reservoir resistivity. However, theoretically simulating these reservoir parameters under formation conditions is still challenging. Previous studies only revealed the effects of predominately pore–fracture parameters on reservoir resistivity. In this study, the influence characteristics of the pore shape changes on the resistivity of rocks saturated with petroleum or water were investigated. Nevertheless, measuring the extension direction of the pores in the formation is constrained by the existing well logging technology. Hence, future theoretical simulations should focus on important geological factors (i.e., temperature and pressure of formation) and hydrocarbon saturation.

5. Conclusions

Based on the principles of electrical well logging and Ohm's Law, electrical conductivity models were developed for both vuggy and fractured carbonate reservoirs. Mathematical expressions for resistivity were derived for different reservoir types, and the deep laterolog resistivity responses in carbonate reservoirs were numerically simulated. The effects of fractured–cavernous structural parameters on rock resistivity were examined.

For porous reservoirs, univariate simulation suggests that as the throat diameter increases, the rock resistivity declines in a triphasic manner. Only changes in pore dimensions along the direction of the current have a significant effect on reservoir resistivity. The formation water and rock matrix resistivity have a stronger effect on the resistivity of oil-saturated rocks than water-saturated rocks. As the water film thickness increased, the resistivity of oil-saturated rocks decreased in a triphasic manner. In all, the throat diameter was the primary factor affecting the resistivity when changes in the rock matrix and formation water resistivity were insignificant. The second most important factor was pore shape, particularly the extension of pores in the direction of the current, which can severely reduce the resistivity of oil-saturated rocks.

For fractured reservoirs, univariate simulation indicates that as the fracture inclination angle or formation water resistivity increases or the fracture width decreases, the rocks with water-saturated fractures increase in resistivity more than rocks containing oil-saturated fractures. In cases where the fractures are saturated with oil, the variations in fracture parameters have no effect on rock resistivity. However, as matrix porosity increases, rock resistivity decreases in a triphasic manner. The degree of resistivity reduction was more pronounced for rocks with oil-saturated fractures compared to those with water-saturated fractures.

The rock cementation exponent m increased gradually with increasing porosity, although the rate of increase slowed as porosity continued to rise. Pores with a longer major axis along the direction of the current had smaller m values. As fracture width and throat diameter increased, the value of m decreased. The m value was much smaller when the matrix pores were interconnected through fractures than when they were interconnected through throats.

Author Contributions: Conceptualization, C.G.; Methodology, Z.Z., C.G. and Y.G.; Software, C.N. and S.M.; Formal analysis, Y.G.; Investigation, Z.Z. and S.M.; Data curation, C.N. and S.M.; Writing—original draft, Z.Z.; Visualization, Y.G.; Project administration, C.G.; Funding acquisition, Z.Z. All authors have read and agreed to the published version of the manuscript.

Funding: This research was funded by Initial Scientific Research Foundation of Xinjiang University for Doctors (No. 620321016); the Research Foundation of Tianchi Outstanding Doctors (No. 51052300560); and the Open Fund of Key Laboratory of Petroleum Resources Research, Gansu Province (No. SZDKFJJ2023007).

Data Availability Statement: All data used to support the findings of this study are included with the article.

Acknowledgments: We express our gratitude to the editors and anonymous reviewers for their informative and constructive feedback.

Conflicts of Interest: Author Yongde Gao was employed by the company CNOOC Limited. The remaining authors declare that the research was conducted in the absence of any commercial or financial relationships that could be construed as a potential conflict of interest.

References

1. Bust, V.K.; Oletu, J.U.; Worthington, P.F. The challenges for carbonate petrophysics in petroleum resource estimation. *SPE Reserv. Eval. Eng.* **2011**, *14*, 25–34. [CrossRef]
2. Xu, T.; Lindsay, G.; Zheng, W.; Baihly, J.; Ejofodomi, E.; Malpani, R.; Shan, D. Proposed refracturing-modeling methodology in the haynesville shale, a US unconventional basin. *SPE Prod. Oper.* **2019**, *34*, 725–734. [CrossRef]
3. Organization of the Petroleum Exporting Countries. *World Oil Outlook 2045*; Organization of the Petroleum Exporting Countries: Vienna, Austria, 2022.
4. Wang, D.B.; Zhou, F.J.; Li, Y.P.; Yu, B.; Martyushev, D.; Liu, X.F.; Wang, M.; He, C.M.; Han, D.X.; Sun, D.L. Numerical simulation of fracture propagation in Russia carbonate reservoirs during refracturing. *Pet. Sci.* **2022**, *19*, 2781–2795. [CrossRef]
5. Gu, Y.Q.; Liu, W.J.; Wang, B.W.; Tian, B.R.; Yang, X.Y.; Pan, C.C. Analysis and Prediction of Energy, Environmental and Economic Potentials in the Iron and Steel Industry of China. *Processes* **2023**, *11*, 3258. [CrossRef]

6. Li, L.; Xiao, D.; Liu, R.; Zhang, Y.; Shan, S.J.; Liu, Y.; Zhong, J.Y.; Tan, X.C. Origin of breccia dolomites in the middle Devonian Guanwushan Formation, NW Sichuan Basin, China: Implications for ultra-deep carbonate reservoirs. *Geoenergy Sci. Eng.* **2023**, *227*, 211949. [CrossRef]
7. Jia, C.Z.; Zheng, M.; Zhang, Y.F. Unconventional hydrocarbon resources in China and the prospect of exploration and development. *Pet. Explor. Dev.* **2012**, *39*, 129–136. [CrossRef]
8. Li, Y.; Hou, J.G.; Li, Y.Q. Features and classified hierarchical modeling of carbonate fracture-cavity reservoirs. *Pet. Explor. Dev.* **2016**, *43*, 655–662. [CrossRef]
9. Rashid, F.; Glover, P.; Lorinczi, P.; Hussein, D.; Lawrence, J. Microstructural controls on reservoir quality in tight oil carbonate reservoir rocks. *J. Pet. Sci. Eng.* **2017**, *156*, 814–826. [CrossRef]
10. Liu, S.X.; Xue, H.J.; Zhao, M.Y. Pore Structure and Fractal Characteristics of Coal Measure Shale in the Wuxiang Block in the Qinshui Basin. *Processes* **2023**, *11*, 3362. [CrossRef]
11. Sharifi, J.; Moghaddas, N.H.; Saberi, M.R. A novel approach for fracture porosity estimation of carbonate reservoirs. *Geophys. Prospect.* **2023**, *71*, 664–681. [CrossRef]
12. Choquette, P.A.; Pray, L.C. Geologic nomenclature and classification of porosity in sedimentary carbonate. *AAPG Bull.* **1970**, *54*, 207–250.
13. Zhao, L.X. Study of the complex carbonate pore structures. *World Well Logging Technol.* **2014**, *1*, 20–22. (In Chinese)
14. Bjørlykke, K. Relationships between depositional environments, burial history and rock properties. Some principal aspects of diagenetic process in sedimentary basins. *Sediment. Geol.* **2014**, *301*, 1–14. [CrossRef]
15. Mohammed-Sajed, O.K.; Glover, P.W.; Al-Khatony, F.H.; Collier, R.E. Qualitative and quantitative diagenetic modelling in a tight carbonate reservoir in north-western Iraq. *Geoenergy Sci. Eng.* **2024**, *232*, 212450. [CrossRef]
16. Xie, F.; Zhang, C.S.; Liu, R.L.; Xiao, C.W. Production prediction for fracture-vug carbonate reservoirs using electric imaging logging data. *Pet. Explor. Dev.* **2018**, *45*, 349–356. [CrossRef]
17. Ren, J. Conventional logging evaluation method for carbonate fractured reservoir. *Lithol. Reserv.* **2020**, *32*, 129–137.
18. Rabaev, R.; Chibisov, A.; Kotenev, A.; Kotenev, M.; Dubinskiy, G.; Muhametshin, V.; Efimov, E. Mathematical modelling of carbonate reservoir dissolution and prediction of the controlled hydrochloric acid treatment efficiency. *SOCAR Proc.* **2021**, *2*, 40–46. [CrossRef]
19. Rong, Y.S.; Pu, W.F.; Zhao, J.Z.; Li, K.X.; Li, X.H.; Li, X.B. Experimental research of the tracer characteristic curves for fracture-cave structures in a carbonate oil and gas reservoir. *J. Nat. Gas Sci. Eng.* **2016**, *31*, 417–427. [CrossRef]
20. Miller, K.; Vanorio, T.; Keehm, Y. Evolution of permeability and microstructure of tight carbonates due to numerical simulation of calcite dissolution. *J. Geophys. Res. Solid Earth* **2017**, *122*, 4460–4474. [CrossRef]
21. Mao, Z.Q.; Gao, C.Q. Theoretical simulation of the resistivity and pore structure of hydrocarbon bearing rocks. *Pet. Explor. Dev.* **2000**, *27*, 87–90.
22. Stadtműller, M.; Krakowska-Madejska, P.I.; Leśniak, G.; Jarzyna, J.A. Characterization of the carbonate formation fracture system based on well logging data and results of laboratory measurements. *Energies* **2021**, *14*, 6034. [CrossRef]
23. Stadtműller, M.; Jarzyna, J.A. Estimation of petrophysical parameters of carbonates based on well logs and laboratory measurements, a review. *Energies* **2023**, *16*, 4215. [CrossRef]
24. Rathinasamy, V.; Mohamad, E.T.; Komoo, I.; Legiman, M.K.A.; Amaniyah, N.; Bhatawdekar, R.M.; Hanapi, M.N.B.; Suparmanto, E.K.B. Fracture characterization using downhole camera in deep boreholes at Southern Johor Bahru, Malaysia. In *Proceedings of the Geotechnical Challenges in Mining, Tunneling and Underground Infrastructures*; Lecture Notes in Civil Engineering; Springer: Singapore, 2022; Volume 228.
25. Yang, Y.F.; Tao, L.; Yang, H.Y.; Iglauer, S.; Wang, X.; Askari, R.; Yao, J.; Zhang, K.; Zhang, L.; Sun, H. Stress Sensitivity of Fractured and Vuggy Carbonate: An X-Ray Computed Tomography Analysis. *JGR Solid Earth* **2020**, *125*, e2019JB018759. [CrossRef]
26. Aguilera, R. Analysis of naturally fractured reservoirs from conventional well logs. *J. Pet. Technol.* **1976**, *28*, 764–772. [CrossRef]
27. Bauer, D.; Youssef, S.; Fleury, M.; Bekri, S.; Rosenberg, E.; Vizika, O. Improving the estimations of petrophysical transport behavior of carbonate rocks using a dual pore network approach combined with computed microtomography. *Transp. Porous Media* **2012**, *94*, 505–524. [CrossRef]
28. He, J.H.; Li, M.; Zhou, K.M.; Yang, Y.; Xie, B.; Li, N.; Dang, L.R.; Tang, Y.B. Effects of vugs on resistivity of vuggy carbonate reservoirs. *Pet. Explor. Dev.* **2020**, *47*, 490–498. [CrossRef]
29. Aguilera, M.S.; Aguilera, R. Improved models for petrophysical analysis of dual porosity reservoirs. *Petrophysics* **2003**, *44*, 21–35.
30. Liu, R.L.; Li, N.; Feng, Q.F.; Hai, C.; Wang, K.W. Application of the triple porosity model in well-log effectiveness estimation of the carbonate reservoir in Tarim Oilfield. *J. Pet. Sci. Eng.* **2009**, *68*, 40–46. [CrossRef]
31. Katz, A.J.; Thompson, A.H. Fractal sandstone pores: Implications for conductivity and pore formation. *Phys. Rev. Lett.* **1985**, *54*, 1325–1328. [CrossRef]
32. Adler, P.M.; Thovert, J.-F. Fractal porous media. *Transp. Porous Media* **1993**, *13*, 41–78. [CrossRef]
33. Berg, C.R. Dual-porosity equations from effective medium theory. In Proceedings of the SPE Annual Technical Conference and Exhibition, San Antonio, TX, USA, 24–27 September 2006; p. 101698.
34. Leverett, M.C. Capillary behavior in porous solids. *Trans. AIME* **1940**, *142*, 159–172. [CrossRef]
35. Yuan, H.H. Relationship between permeability and factors "A" "M" in Archie equation-capillary theory in the study of rock resistivity. *Well Logging Technol.* **1990**, *14*, 40–45. (In Chinese)

36. Winsauer, W.O. Resistivity of brine-saturated sands in relation to pore geometry. *AAPG Bull.* **1952**, *36*, 230–252.
37. Fu, J.L.; Thomas, H.R.; Li, C.F. Tortuosity of porous media: Image analysis and physical simulation. *Earth-Sci. Rev.* **2021**, *212*, 103439. [CrossRef]
38. Greenberg, R.J.; Brace, W.F. Archie's law for rocks modeled by simple networks. *J. Geophys. Res.* **1969**, *74*, 2099–2102. [CrossRef]
39. Xiong, Q.R.; Baychev, T.G.; Jivkov, A.P. Review of pore network modelling of porous media: Experimental characterisations, network constructions and applications to reactive transport. *J. Contam. Hydrol.* **2016**, *192*, 101–117. [CrossRef] [PubMed]
40. Wang, K.W.; Sun, J.M.; Guan, J.T.; Su, Y.D. Percolation network modeling of electrical properties of reservoir rock. *Acta Pet. Sin.* **2007**, *28*, 101–106. (In Chinese) [CrossRef]
41. Kirkpatrick, S. Classical transport in disordered media: Scaling and effective-medium theories. *Phys. Rev. Lett.* **1977**, *27*, 1722–1728. [CrossRef]
42. Ghanbarian, B.; Daigle, H. Permeability in two component porous media: Effective-medium approximation compared with lattice-Boltzmann simulations. *Vadose Zone J.* **2016**, *15*, 1–10. [CrossRef]
43. Wang, Y.M.; Sharma, M.M. A network model for the resistivity behavior of partially saturated rocks. In Proceedings of the 29th Annual Logging Symposium Transactions: Society of Professional Well Log Analysts, San Antonio, TX, USA, 5–8 June 1988.
44. Yuan, C.; Li, C.L.; Zhou, C.C.; Xiao, Q.Y.; Li, X.; Fan, Y.R.; Yu, J.; Wang, L.; Xing, T. Forward simulation of array laterolog resistivity in anisotropic formation and its application. *Pet. Explor. Dev.* **2020**, *47*, 77–85. [CrossRef]
45. Lai, Q.; Tang, J.; Wu, Y.Y.; Xu, W.; Xie, B.; Jin, Y. Numerical simulation and resistivity anisotropic correction method of dual laterolog response in highly deviated well. *Oil Geophys. Prospect.* **2022**, *57*, 706–712.
46. Subbit, A.M.; Faivre, O. The Dual laterolog response in fractured rock. In Proceedings of the Dallas Texas: SPWLA 26th Annual Logging Symposium, Dallas, TX, USA, 17–20 June 1985; pp. 17–20.
47. Wang, H.M.; Zhang, G.J.; Li, S.J.; Liu, F.P. The dual laterolog response of the single dipping fracture. *J. Univ. Pet.* **1995**, *19*, 21–24.
48. Li, S.J.; Xiao, C.W.; Wang, H.M.; Zang, G.J. Mathematical model of dual laterolog response of fractures and quantitative interpretation of fracture porosity. *J. Geophys.* **1996**, *39*, 845–852. [CrossRef]
49. Shi, G.; He, T.; Wu, Y.Q.; Liu, J.H.; Ma, Y. A study on the dual laterolog response to fractures using the forward numerical modeling. *Chin. J. Geophys.* **2004**, *47*, 359–363.
50. Deng, S.G.; Mo, X.X.; Lu, C.L.; Zhang, Y.; Liu, L.L. Numerical simulation of the dual laterolog response to fractures and caves in fractured–cavernous formation. *Pet. Explor. Dev.* **2012**, *39*, 706–712. [CrossRef]
51. Ge, X.M.; Fan, Y.R.; Li, J.; Tan, B.H.; Wang, L.; Wu, Z.G.; Wang, X.C. Experimental studies and investigations on the dual lateral log response of near borehole fractures. *Chin. J. Geophys.* **2019**, *62*, 354–360.
52. Bai, Y.; Luo, P.; Wang, S.; Zhou, C.M.; Zhai, X.F.; Wang, S.; Yang, Z.Y. Structure characteristics and major controlling factors of platform margin microbial reef reservoirs: A case study of Xiaoerbulak Formation, Lower Cambrian, Aksu area, Tarim Basin, NW China. *Pet. Explor. Dev.* **2017**, *44*, 349–358. [CrossRef]
53. Zhang, Y.F.; Tan, F.; Qu, H.Z.; Zhong, Z.Q.; Liu, Y.; Luo, X.S.; Wang, Z.Y.; Qu, F. Karst monadnock fine characterization and reservoir control analysis: A case from Ordovician weathering paleokarst reservoirs in Lungu area, Tarim Basin, China. *Pet. Explor. Dev.* **2017**, *44*, 716–726. [CrossRef]
54. Liu, Y.M.; Hou, J.G.; Li, Y.Q.; Dong, Y.; Ma, X.Q.; Wang, X.X. Characterization of architectural elements of Ordovician Fractured–cavernous carbonate reservoirs, Tahe Oilfield, China. *J. Geol. Soc. India* **2018**, *91*, 315–322. [CrossRef]
55. Kirkpatrick, S. Percolation and conduction. *Rev. Mod. Phys.* **1973**, *45*, 574–588. [CrossRef]
56. Archie, G.E. The electrical resistivity log as an aid in determining some reservoir characteristics. *Trans. AIME* **1942**, *146*, 54–61. [CrossRef]
57. Zhang, Z.H.; Yu, H.G.; Chen, H.Y.; Du, S.K.; Li, C. Quantitative characterization of fracture-pore distribution and effects on production capacity of weathered volcanic crust reservoirs: Insights from volcanic gas reservoirs of the Dixi area, Junggar Basin, Western China. *Mar. Pet. Geol.* **2022**, *140*, 105651. [CrossRef]
58. Schmoker, J.W.; Hally, R.B. Carbonate porosity versus depth: A predictable relation for South Florida. *AAPG Bull.* **1988**, *66*, 2561–2570.
59. Ehrenberg, S.N.; Nadeau, P.H.; Steen, Ø. Petroleum reservoir porosity versus depth: Influence of geological age. *AAPG Bulletin* **2009**, *93*, 1281–1296. [CrossRef]
60. Ehrenberg, S.N. Factors controlling porosity in upper carboniferous–lower Permian carbonate strata of the barents sea. *AAPG Bull.* **2004**, *88*, 1653–1676. [CrossRef]
61. Wennberg, O.P.; Casini, G.; Jonoud, S.; Peacock, D.C. The characteristics of open fractures in carbonate reservoirs and their impact on fluid flow: A Discussion. *Pet. Geosci.* **2016**, *22*, 91–104. [CrossRef]
62. Mohammed-Sajed, O.K.; Glover, P.W.J. Dolomitisation, cementation and reservoir quality in three Jurassic and Cretaceous carbonate reservoirs in north-western Iraq. *Mar. Pet. Geol.* **2020**, *115*, 104256. [CrossRef]
63. de Lima, A.; Lopes, J.A.; Medeiros, W.E.; Schiozer, D.J.; La Bruna, V.; Bezerra, F.H. Impact of fracture set scales and aperture enlargement due to karstic dissolution on the fluid flow behavior of carbonate reservoirs: A workflow to include sub-seismic fractures in 3D simulation models. *Geoenergy Sci. Eng.* **2023**, *221*, 211374. [CrossRef]
64. Tian, H.; Shen, A.J.; Zhang, J.Y.; Feng, Q.F.; Wang, H.; Xin, Y.G.; Li, W.Z.; Li, C.; Tian, M.Z.; Zhang, H. New calculation method of cementation exponent m for crack-vuggy carbonate reservoirs. *Chin. J. Geophys.* **2019**, *62*, 2276–2285.

65. Lü, X.X.; Wang, Y.F.; Yu, H.F.; Bai, Z.K. Major factors affecting the closure of marine carbonate caprock and their quantitative evaluation, A case study of Ordovician rocks on the northern slope of the Tazhong uplift in the Tarim Basin, western China. *Mar. Pet. Geol.* **2017**, *83*, 231–245. [CrossRef]
66. Ouyang, S.Q.; Lü, X.X.; Quan, H.; Awan, R.S.; Zhou, J.X.; Wang, R. Evolution process and factors influencing the tight carbonate caprock: Ordovician Yingshan Formation from the northern slope of the Tazhong uplift, Tarim Basin, China. *Mar. Pet. Geol.* **2023**, *147*, 105998. [CrossRef]